Dynamics of Atmospheres and Oceans, 20 (1993) 55–77
Elsevier Science Publishers B.V., Amsterdam

A 2-D complex wavelet analysis of an unsteady wind-generated surface wave field

G.R. Spedding *[,a], F.K. Browand [a], N.E. Huang [b], S.R. Long [b]

[a] *Department of Aerospace Engineering, University of Southern California, Los Angeles, CA 90089-1191, USA*

[b] *Air–Sea Interaction Research Facility, NASA Wallops Field, Wallops Island, VA 23337, USA*

(Received 18 May 1992; revised 15 December 1992; accepted 15 December 1992)

ABSTRACT

Nonlinear wave–wave interactions can be quite localised in space and an appropriate spectral analysis of such a wave field must retain this local phase information. To this end, the 2-D, complex wavelet functions 'Arc' and 'Morlet2D' can be used to decompose a wave field in space $\boldsymbol{b}$ and scale a. As both wavelets are Hardy functions, the transform result is complex, and the phase, ϕ, is defined over all $\boldsymbol{b}$. Arc can be used to measure the energy of the wave field over $\boldsymbol{b}$ as a function of $|\boldsymbol{k}|$, and the direction-specific wavelet, Morlet2D, can be used for the spatial energy distribution of $\boldsymbol{k}$.

Surface waves generated by unsteady wind have dislocations in phase that are widespread and persist until the initial wave field becomes disordered in appearance. While the energy at fundamental wavelengths (the wavelength of the initial instability) appears to saturate, the energy of the subharmonic component continues to increase with time. There appears to be significant energy in both modes, from early on in the life history of these organised wave fields. The energy of wavevectors aligned at a small angle off the mean wind direction vector (the including angle, $\alpha \approx 20°$) increases to become a substantial fraction of the total energy. The possible role of the pattern defects in local nonlinear mechanisms of energy transfer is discussed, and analogies are drawn with recent results in plane mixing layers. Techniques for the measurement of the complex dispersion relation, $\omega(\boldsymbol{k})$, and group velocity, $\boldsymbol{U}_g(\boldsymbol{k})$, utilising the local space-scale decomposition of the 2D wavelet transform, are proposed.

1. INTRODUCTION

Microscale capillary–gravity waves are responsible both for a large portion of the momentum and energy transfer across the air–water interface and for the Bragg scattering and detection of surface features by remote sensing devices. Their generation by wind is therefore of critical importance in quantifying fluxes across the air–sea interface, and in deter-

* Corresponding author.

mining the transmission and detection of pattern information to microwave remote sensors. The review by Phillips (1988) and the recent volumes by Geerneart and Plant (1990) may be consulted for details.

Thus far, classical linear instability analysis (see Phillips, 1957, 1977 and Miles, 1957, 1959) has had somewhat limited success in accounting for laboratory data that are becoming increasingly sophisticated and quantitative, and that showing growth rates that differ markedly from theoretical values (Wu et al., 1979; Snyder et al., 1981) and also demonstrating the strongly nonlinear nature of the interactions between modes (e.g. Okuda, 1982a–c). One such possible interaction would be the wave-crest pairing event discussed by Ramamonjiarisoa and Mollo-Christensen (1979), or perhaps 'wave-trough pairing' as suggested by Melville (1983). Not only is it apparent that nonlinear mechanisms can be important, if not dominant, but, as pointed out by Melville (1983), for example, there is a clear need for a spectral analysis that satisfactorily accounts for both phase and amplitude modulations in wave fields where nonlinear wave interactions give rise to variation in both frequency and wavenumber.

Given the complexity of the phenomena observed in the field, one turns to carefully controlled laboratory experiments, where attention will be focused on the wave–wave interactions in an unsteady wave field generated by a time-dependent wind stress. Informal observations show complex pattern deformations that appears very early on in the generation of surface roughness. The wave field then rapidly becomes very disorganised in appearance. The mechanisms reponsible for this transition from regular to disordered surface wave motions are as yet poorly understood.

The investigation described here is an initial attempt to apply certain recently developed wavelet transform analytical tools to obtain a space-scale decomposition of a two-dimensional (2-D) surface wave field. Although the current analysis is preliminary in nature, the careful application of 2-D complex wavelet transforms allows one to perform a quantitative, whole-field, unsteady analysis. The overall objectives are to identify and quantify the (nonlinear) dynamics responsible for the pattern generation and the eventual disruption in surface roughness generated by unsteady wind.

2. 2-D WAVELET TRANSFORM

2.1. Definitions and background

Wavelet transform analysis, after its initial introduction and formalisation by Grossmann and Morlet (1984), has enjoyed considerable success in signal and image processing and analysis, and as an efficient basis for computing numerical solutions of systems of partial differential equations

(see Combes et al. (1989) for an overview). This is in part due to the rigorous mathematical basis and also to the systematic way in which the window aperture is automatically varied with scaling parameter, a. In this respect, it differs significantly from the various alternative windowed-Fourier transform and filter techniques.

The extension of the usual definitions of wavelet functions in one dimension to the 2-D case and their application to experimental data in fluid mechanics applications has been considered in some detail by Dallard and Spedding (1993). The general extension of wavelet functions to two dimensions has been discussed by Murenzi (1989). An application of the complex, 2-D Morlet wavelet to analysis of coherent structures in 2-D turbulence has been described by Farge and Rabreau (1988). Dallard and Browand (1993) have reported extensive results from phase-averaged 2-D velocity fields in an acoustically forced mixing layer, and Spedding et al. (1993) have discussed the design and application of 2-D wavelets to 2-D fluid turbulence data. Fluid turbulence applications, including 2-D, have been reviewed by Farge (1992). The important properties of the wavelet functions 'Arc' and 'Morlet2D' will be summarised below, and Dallard and Spedding (1993) may be consulted for a more complete discussion.

In two dimensions, the wavelet transform (WT) of f is the inner product of f with the wavelet $g_{a,b}$,

$$f_{\mathrm{W}}(a, \boldsymbol{b}) = \int\int f(\boldsymbol{r}) \cdot g^*_{a,\boldsymbol{b}}(\boldsymbol{r})\, \mathrm{d}\boldsymbol{r} \tag{1}$$

where g^* is the complex conjugate of g. g is rescaled by a and translated in physical space, $\boldsymbol{b}$, so

$$f_{\mathrm{W}}(a, \boldsymbol{b}) = \frac{1}{a^2} \cdot \int\int f(\boldsymbol{r}) \cdot g^*\left(\frac{\boldsymbol{r} - \boldsymbol{b}}{a}\right) \mathrm{d}\boldsymbol{r} \tag{2}$$

The normalisation by $1/a^2$ ensures that $|(f_{\mathrm{W}}(a, \boldsymbol{b})| \propto |f|$. In practice, it is convenient to work in Fourier space, where the transform can be written

$$f_{\mathrm{W}}(a, \boldsymbol{b}) = \int\int \hat{f}(\boldsymbol{k}) \cdot \hat{g}^*(a\boldsymbol{k}) \exp(i\boldsymbol{k} \cdot \boldsymbol{b})\, \mathrm{d}\boldsymbol{k} \tag{3}$$

2.2. The choice of wavelet function—real vs. complex wavelets

Typically, the wavelet function $g(\boldsymbol{r})$ is some kind of smoothly varying wavepacket inside a Gaussian envelope, and the length scale of the oscillations and wavepacket size (and so, sampling area) vary according to

a. The WT can be seen to be just a decomposition of f onto the family of wavelet basis functions $g_{a,b}$ generated over a range of scales a. There are various possible choices for g, one of the more common being the Mexican Hat function,

$$g(\boldsymbol{r}) = (r^2 - 1)\exp(-r^2/2) \tag{4}$$

However, it is simple to show that the WT derived from such a real function will contain a mixture of amplitude and phase information that can be hard, if not misleading, to interpret. Fluctuations in $|f_W(a, \boldsymbol{b})|$ may be due to modulations in either phase or amplitude of the original signal, and in many non-trivial applications, it may not be obvious which. There is, furthermore, a related difficulty in distinguishing artefacts caused by interference between (oscillatory) nonzero resonances of neighbouring $|f_W(a, \boldsymbol{b})|$ with only small separations in a, $\boldsymbol{b}$.

This point is neither new (see Grossmann and Morlet (1984) and Grossmann et al. (1989); also Liandrat and Moret-Bailly, (1990), for a particularly clear discussion), nor difficult, yet it is frequently ignored. It can be rendered moot by choosing a complex wavelet function satisfying $\hat{g}(\boldsymbol{k}) = 0$ for $\boldsymbol{k} \leqslant 0$. The WT is then complex and may be expressed as a modulus and phase. (For the first and definitive discussion of this topic, see Grossmann and Morlet (1984).)

Within the class of Hardy functions, two have proven useful to this work. In the first case, g is chosen to be direction specific, as in the straightforward extension to two dimensions of the Morlet wavelet,

$$g_\alpha(\boldsymbol{r}) = \exp(i\boldsymbol{k}_0 \cdot \boldsymbol{r}) \cdot \exp(-|\boldsymbol{r}|^2/2) \tag{5}$$

with $5 < \boldsymbol{k}_0 < 6$ fixed and $(\overrightarrow{\boldsymbol{e}_x, \boldsymbol{k}_0}) = \alpha$. This function (Fig. 1), denoted 'Morlet2D', is direction specific, interrogating wavevectors in Fourier space with a preferred magnitude and orientation. Its Fourier transform is

$$\hat{g}_\alpha(\boldsymbol{k}) = \exp\left[-\left(|\boldsymbol{k} - \boldsymbol{k}_0|^2\right)/2\right] \tag{6}$$

Alternatively, 'Arc' (Fig. 2) is both complex and non-directional, and is defined as

$$\boldsymbol{k} \in \pi^1 : \hat{g}_c(\boldsymbol{k}) = \exp\left[-\left(|\boldsymbol{k}| - |\boldsymbol{k}_0|\right)^2/2\right]$$

$$\boldsymbol{k} \in \pi^2 : \hat{g}_c(\boldsymbol{k}) = 0 \tag{7}$$

It should be noted that wavenumber space is partitioned into two halves, π^1 and π^2, and care must be taken to partition the space without bisecting regions of high signal amplitude. This is a simple matter when the wavevec-

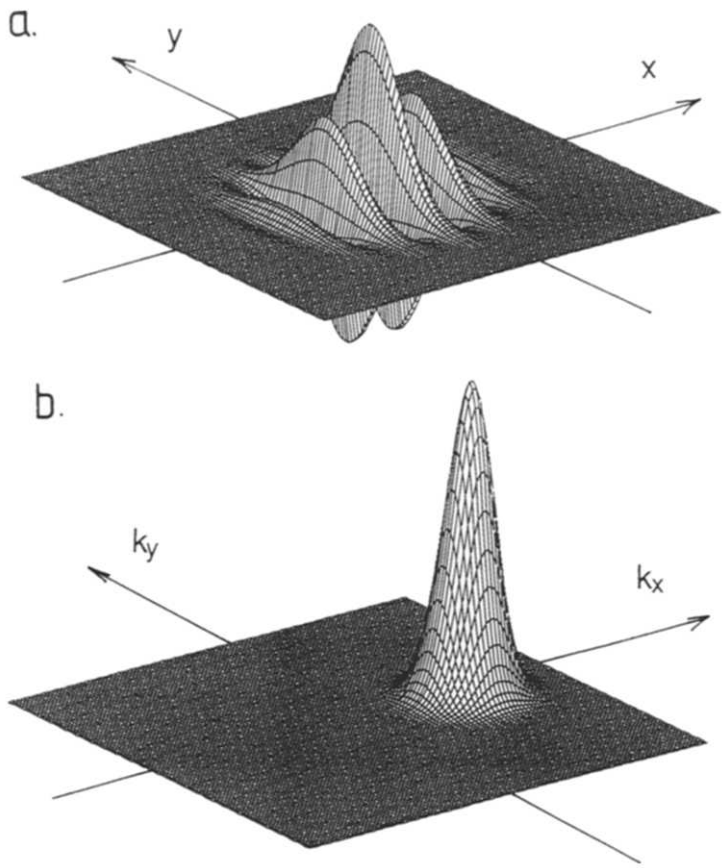

Fig. 1. (a) The real part of the Morlet2D wavelet. (b) The Fourier transform of Morlet2D.

tors are clustered around some relatively localised region in $\boldsymbol{k}$-space, as is the case here.

2.3. Energy measures

The energy and energy density can be computed from the WT as

$$\| f \|^2 = \frac{2}{C_g} \int_{a=0}^{+\infty} \int\int \| f_{\mathrm{W}}(a, \boldsymbol{b}) \|^2 \frac{\mathrm{d}a}{a} \cdot \mathrm{d}\boldsymbol{b} \tag{8}$$

where

$$C_g = \int\int_{k=0}^{+\infty} \frac{|\hat{g}(\boldsymbol{k})|^2}{|\boldsymbol{k}|^2} \mathrm{d}\boldsymbol{k} < +\infty \tag{9}$$

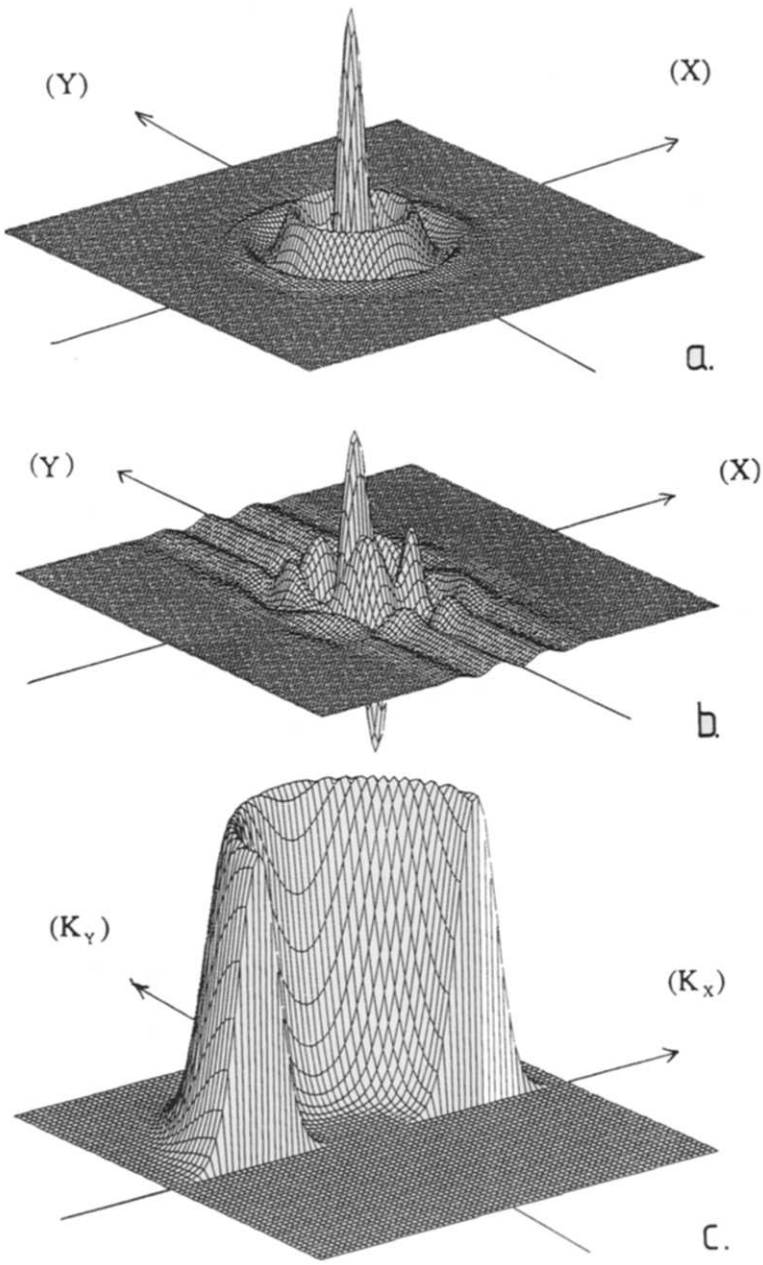

Fig. 2. The real (a) and imaginary (b) parts of the Arc wavelet and its Fourier transform (c).

This is the admissibility condition on the wavelet and amounts to the requirement that $\int\int g(\boldsymbol{r})\, \mathrm{d}\boldsymbol{r} = \hat{g}(\boldsymbol{0}) = 0$.

$(2/C_g) \| f_W(a, \boldsymbol{b}) \|^2$ in Eqn. (8) can be regarded as a spatial energy density (energy per unit area) at the scale a (per unit d(ln a)).

3. MATERIALS AND METHODS

3.1. Experimental facilities

Experiments were conducted in the Air–Sea Interaction Research Facility at NASA Wallops Field. The wave-tank–wind tunnel assembly has a working section of 18.29 m × 1.22 m × 0.91 m (width), where surface wind is generated in a closed-loop tunnel by fan suction. A video camera records disturbances on the water surface at a location 14 m from the upstream end of the quiescent water surface. The water depth is 75 cm, and the enclosed air height is 50 cm.

The air flow is started from rest to 3.4 m s^{-1} (as measured 10 cm above the water surface), which, after some short time (about 6 s from the first noticeable perturbation from resting state; as the flow start-up is not instantaneous, there is some difficulty in defining a time origin here), causes disturbances with wavelengths of the order of 1.5–2 cm to appear in the field of view of the video camera (Fig. 3). For approximately 4 s there is a regime where organised waves are clearly visible, together with dislocations in their structure. The field then becomes very disorganised in appearance, and is replaced after about another 4 s by fetch-limited waves of much longer wavelength. Attention here will be confined to the short interval from the first appearance of the organised wave field to its disappearance (at least to the eye) into apparently incoherent surface motions.

3.2. Data characteristics and image processing

3.2.1. Data representation

The data thus comprise a series of 8-bit grey-scale digitised video images, where there is some unknown mapping between the wave height and/or slope and the grey level. The lighting was diffuse, and from above, and the video camera was also mounted above the surface; also, there is no guarantee that the mapping is unique. However, in the absence of any other information we shall assume that the image brightness is related in some simple but unknown way to the surface slope. This restriction places rather severe limits on the scope of the results, which must therefore be considered preliminary in nature. Comments and interpretation must therefore also be restricted to those of a comparative nature, so that although one may talk of the relative growth and decay of spectral components, their absolute amplitudes and energies are not known.

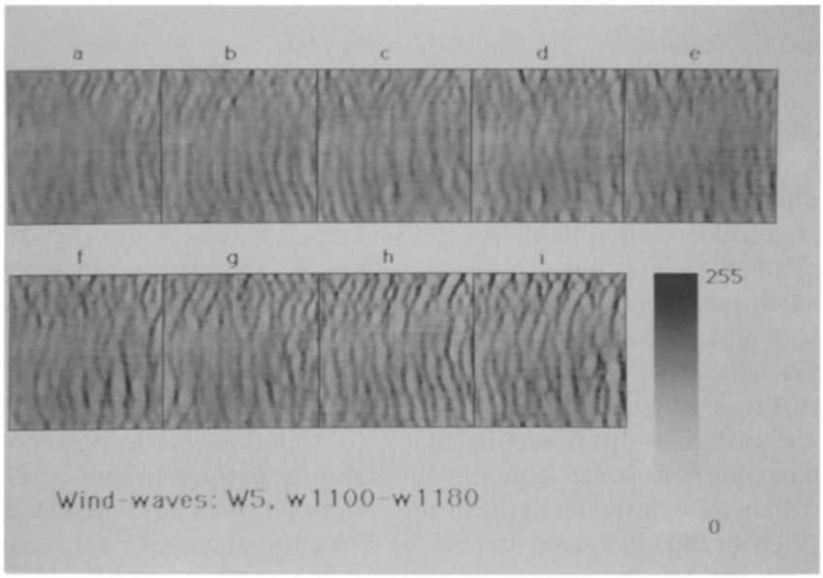

Fig. 3. Sequence of nine rectified video images that comprise the data set for the analysis. The inverse colour bar shows waves as dark stripes on a light background. The longitudinal streaks are thought to be the surface disturbance caused by stream-direction structures in the turbulent boundary layer. The horizontal dimension of each image covers 20 cm, and the time between successive images is 1/3 s. In each image, and in all subsequent wavefield plots, the flow is from right to left, and the original wind forcing is parallel to the x axis, which lies along the horizontal in this figure.

3.2.2. Resolution

Video recordings originally made on Super VHS videotape were transferred to 3/4 in format on a Sony VO-9600 VCR, and digital frame codes were superimposed in the horizontal blanking interval of the video signal. Commercial video frame rates are approximately 30 frames s^{-1}, with successive interleaved fields being separated by 1/60 s. The mean surface wave phase velocity at this wind speed was about 32 cm s^{-1} and so a wave travels roughly 0.5 cm in this time. At any fixed point in space, the phase will therefore change by less than π radians between successive fields, thus satisfying the Nyquist sampling criterion, but with little room for variation. It is entirely possible that the data are undersampled in certain spatial locations, and further quantitative investigations will need to bear this in mind. In commercial video-format charge-coupled device cameras, the top left corner pixel is interrogated just less than one field time before the bottom right pixel, and so there is a consistent aliasing of the signal from

corner to corner, of about one-third wavelength in magnitude. This has not been corrected for in the processed images, which were corrected only for the oblique camera mounting.

3.2.3. Image processing

Each 512×480 digitised image was separated into odd and even fields, the alternate missing lines being filled by bilinear interpolation in the vertical direction only. Simple geometric distortions could be corrected by digitising 10 corner points on the distorted image of a rectangular grid of known dimensions and solving for the coefficients of two second-order polynomial interpolating functions with a least-squares SVD (Singular Value Decomposition) algorithm. The field images were interpolated onto a 512^2 array, smoothed with an eight-neighbour mean filter, and reduced to a 256^2 array (largely to reduce excessive computation times in the wavelet analysis). The edge 10 pixels were then removed to leave two 236^2 rectified images. This is the form of the images in Fig. 3.

3.3. Wavelet analysis

3.3.1. Range of scales

A typical image contains 11 waves over 236 discrete points, and so contains a wavelength approximately every 21 points. In discrete data units, the maximum resonance of the WT with a structure of wavelength λ will be at the scale value $a = (\boldsymbol{k}_0/2\pi)\lambda = 0.875\lambda$, for $|\boldsymbol{k}_0| = 5.5$ (see Eqns. (6) and (7)). Anticipating the results somewhat, fundamental wavelengths may therefore be expected to be detected at $a = 19$, and their subharmonic (if present) at $a = 38$. At analysing scales of $a < 4$, the transform results may be contaminated by noise and/or smoothing in the data, and the largest available a is limited by the support of the wavelet. At $a = 50$, the transform is free of artefacts from the edge effects (assumption of periodicity) only in a central $236 - 100 = 136$ square. A compromise solution to retain as much information on likely large scales and minimise the risk of significant artefacts from the edge effects was to perform the analysis on the entire 236^2 array, but retain only the central 180^2 of the result. Finally, as the resolution of the wavelet varies logarithmically with a, sufficient resolution in a can be achieved by choosing 40 logarithmically spaced values over the range $6 \leqslant a \leqslant 50$, a range of about four octaves.

3.3.2. Transform representation—wavelet cubes

The wavelet transform result of the 2-D data in physical coordinates (x, y) is $f_W(a, \boldsymbol{b})$. The horizontal axes of the resulting cube represent the position vector $\boldsymbol{b}$ (equivalent to the x and y spatial coordinates), and the

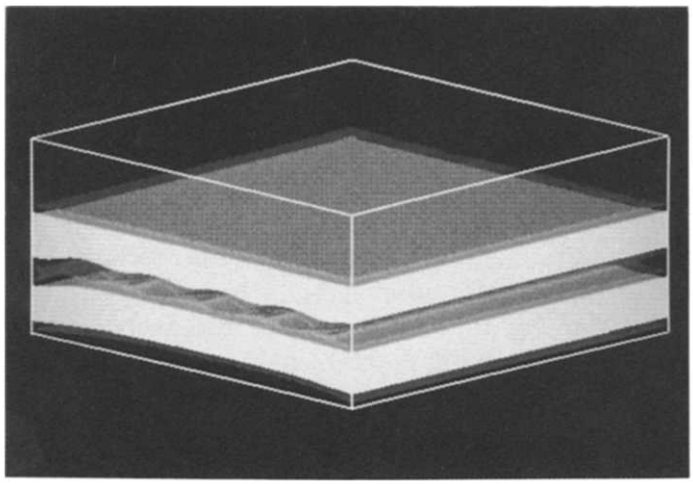

Fig. 4. The modulus of the Arc wavelet transform ($|f_{W_c}(a, \boldsymbol{b})|$) for a test signal composed of two sine waves of equal energy but different frequency. In this, and all subsequent cubes, the horizontal axes are physical space axes x and y, with x the streamwise direction running from the front right face to the back left. The vertical axis is $-\ln a$, so larger scales appear at the base of the cube. The dark and white isocolour surfaces are drawn at 10% and 30% of the modulus maximum.

vertical axis denotes the scale a. As it is actually $-\ln a$, larger scales appear towards the base of the cube. The range of physical length scales from base to top of the cube is from 5.65 to 0.68 cm, or from $2.66\lambda_0$ to $0.37\lambda_0$, where λ_0 is the initial instability wavelength. The transform modulus, $|f_W(a, \boldsymbol{b})|$, gives the amplitude and the argument, $\angle f_W(a, \boldsymbol{b})$, gives the phase at each scale. Results will be plotted as iso-value surfaces of $|f_W(a, \boldsymbol{b})|$ in an otherwise transparent wireframe cube, where the semi-opaque, dark, outer shell represents 10% of the maximum value, and the inner, solid, white surface is drawn at 30% of the maximum.

3.4. Test signal with two frequencies

As an example, Fig. 4 shows the wavelet cube (from the modulus of the Arc transform) that would result if the signal contained two pure sine waves, one with half the frequency of the other, with equal energy in each component. The wavelength of the fundamental was chosen to be equal to the average initial instability wavelength, λ_0, observed in the experiment (after conversion for equivalent pixel resolution). At each scale, almost all the transform energy is contained in bands that are reasonably well separated in a (vertical axis), and have equal width and equal amplitude. It should be noted that the WT of a single frequency is not a delta function,

but is smeared out in a Gaussian distribution centred about that point (see Eqns. (1), (6) and (7)). As this resolution in a can be calculated directly, the total energy, E_λ, at a particular physical length scale, λ, can be recovered by integrating in bands of a about the value $a_\lambda = 0.875\lambda$, over the data area, S:

$$E_\lambda = \frac{1}{S} \cdot \frac{2}{C_g} \int_S \int_{\frac{2}{3}a_\lambda}^{\frac{4}{3}a_\lambda} |f_W(a, \boldsymbol{b})|^2 \, \mathrm{d}\boldsymbol{b} \frac{\mathrm{d}a}{a} \tag{10}$$

There are some artefacts visible in Fig. 4; the two bands are not completely flat as there is a beating resonance between them, and the ends of the subharmonic band are downturned very slightly, because of the assumption of periodicity (deliberately not satisfied in this synthetic signal) at the edges. These effects are thought to be small enough to be tolerable in this case.

4. RESULTS

The complex, 2-D wavelet transform is a powerful quantitative analytical tool for the space-scale decomposition of wind-generated surface waves. This is of special interest when it is suspected that localised nonlinear mechanisms may be responsible for the evolution of these wave fields beyond their initially well-ordered state. In particular, it is possible to measure the spatial distribution of the surface wave spectrum, and the contribution of features that are non-uniform in space can be identified. Such measurements have not hitherto been possible, or have been achieved only with great computational expense and/or ad hoc choices of windowed Fourier transforms. The closest approach appears to have been that of Riemer (1991), some of whose results are shown in Jähne's (1991) excellent monograph on digital image processing. Riemer's use of Gabor filters (Gabor, 1945), however, still requires that an independent choice be made of filter width (and, hence, analysing scale, a), and it is precisely this difficulty that the wavelet transform removes. Based upon observations of the wavelet transform data, three significant conclusions are drawn concerning the developing microscale wave field. Each is discussed separately below.

4.1. Energy is found in both subharmonic and fundamental wavelengths

Figure 5 shows the Arc transform modulus, $|f_{W_c}(a, \boldsymbol{b})|$, from the earliest timestep in the series (Fig. 3(a), where once again, dark gray is the 10% contour and solid white is the 30% contour). Clearly, the energy distribution is quite intermittent in space. Furthermore, appreciable energy can be

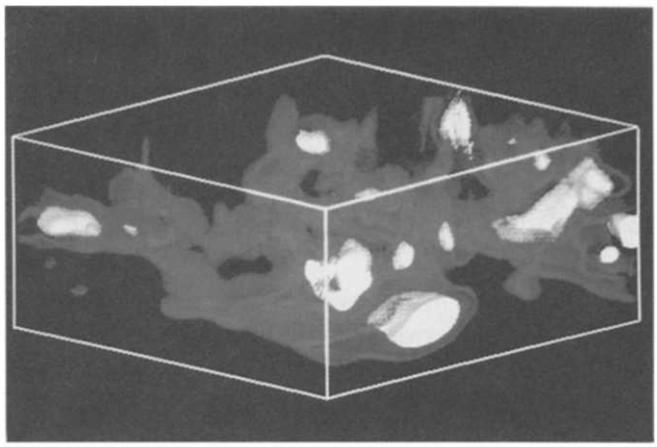

Fig. 5. $|f_{W_c}(a, b)|$ for the data in Fig. 3(a), early in the time sequence. The wind forcing, and main component of the wave energy, is in the direction from the back right panel to the front left face.

observed at both fundamental and subharmonic scales (among others), even at these early times. The white patches, representing the largest amplitude, are scattered rather sparsely. At later times, the white patches occupy a larger fraction of the physical space as the amplitudes grow. It is also clear that the bulk of the energetic features is concentrated about the scales corresponding to the fundamental and subharmonic wavelengths.

The total energy in the fundamental and subharmonic, E_{λ_0}, $E_{2\lambda_0}$, found by integrating over bands about λ_0 and $2\lambda_0$ and then over all space (Eqn. (10)), is plotted as a function of time in Fig. 6. Energy in the fundamental band is seen to grow slowly, then more rapidly, and finally appears to saturate. By contrast, although the energy in the subharmonic band grows more slowly over most of the time interval in question, there is no sign of saturation. At this time, the total energy in the subharmonic is approximately half that of the fundamental.

4.2. Energetic events at fundamental and subharmonic wavelengths occupy different regions of physical space

Another interesting feature of Fig. 5 is that regions of most intense activity at the fundamental scale do not overlap regions active at the subharmonic scale. This conclusion is difficult to draw from one single view, as in Fig. 5, but a number of views shows this to be the case qualitatively. It continues to be true as the wave field develops.

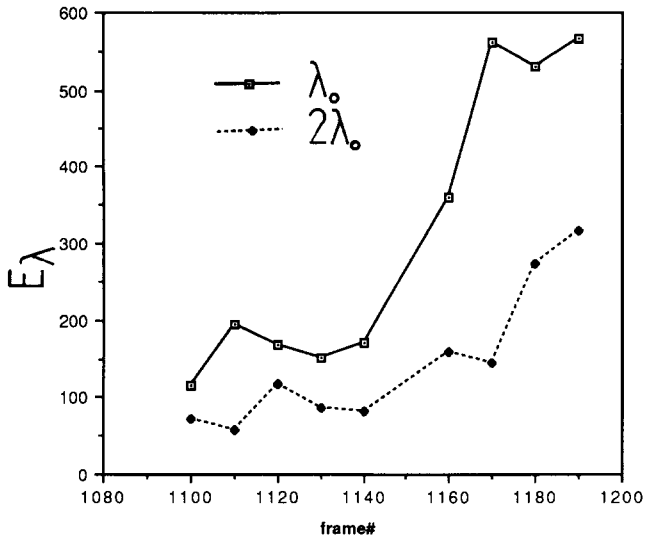

Fig. 6. $E_\lambda(t)$ for the fundamental ($\lambda = \lambda_0$) and subharmonic ($\lambda = 2\lambda_0$) length scales.

In a different context that none the less involves some interesting parallels to this one, Dallard and Browand (1993) showed that, in a plane, turbulent mixing layer, the development of larger scales, centred at the first subharmonic scale, takes place preferentially at defect sites in the fundamental wave pattern. These defect sites were identified as dislocation points in the pattern, and are precisely those points at which the energy of the fundamental is lowest. Yang et al. (1993) explained the behaviour in terms of a nonlinear mechanism which acts to suppress subharmonic growth where the fundamental is strong, but fails to suppress growth where the fundamental is weak.

Here also, many dislocation points can be observed, and it is natural to enquire whether the defects appearing in the surface wave field play a similar role in the interscale energy transfer. Figures 7(a)–7(c) show the isophase-lines for the Arc wavelet transform at an analysing scale, a, corresponding to λ_0, and at the same time, isocontours of $|f_W(a, \boldsymbol{b})|$ for the slice $a = 35$, at $2\lambda_0$. This is done at two times, corresponding to timesteps b (Figs. 7(a) and 7(b)) and f (Figs. 7(c) and 7(d)) in Fig. 3. The postulate of a positive correlation of defects in $\angle f_W(a, \boldsymbol{b})$ at λ_0 with peaks in $|f_W(a, \boldsymbol{b})|$ at $2\lambda_0$ is plausible in the early stages of growth of the surface wave field (Figs. 7(a) and 7(b)), but less clear later on (Figs. 7(c) and 7(d)). Furthermore, in a dispersive wave field, the different phase speeds of the two modes, coupled with the fact that growth is occurring in both spatial and temporal domains, significantly complicates the interpretation of a simple spatial correlation, perhaps even after short times follow-

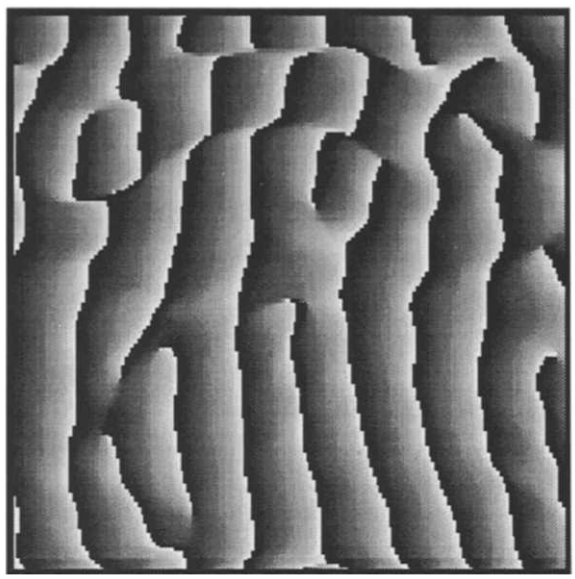

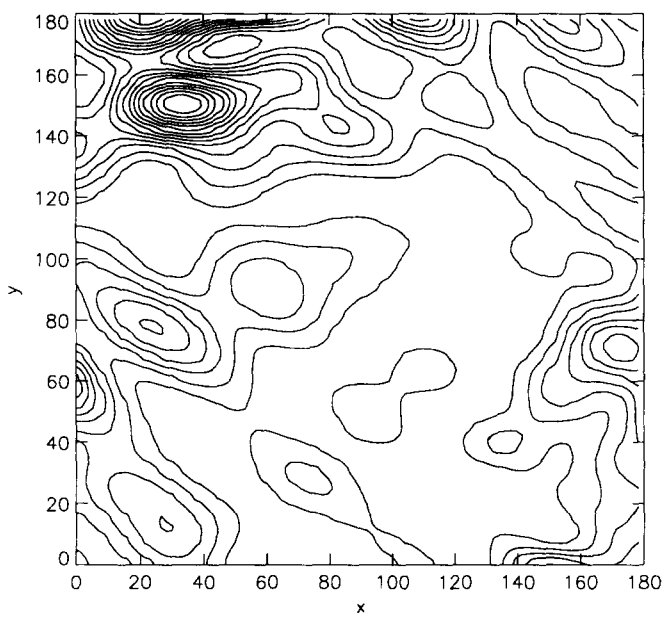

Fig. 7. Phase surfaces for the fundamental mode $\lambda = \lambda_0$, and the corresponding energy at the subharmonic scales, $2\lambda_0$, as shown by contours of $|f_W(a, b)|$ for an early time (A, B) and approximately 1.3 s later (C, D). The contours of $|f_W(a, b)|$ in (B) and (D) have equal spacing, $\Delta|f_W(a, b)|$, linearly spaced over the range of energies at each scale. The units in x and y are millimetres.

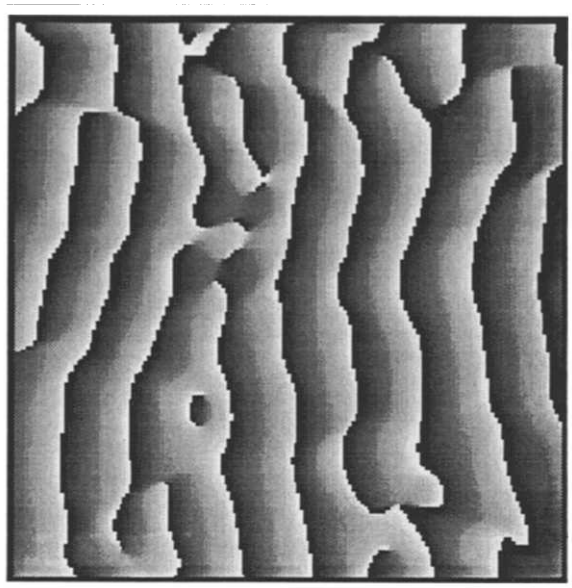

C

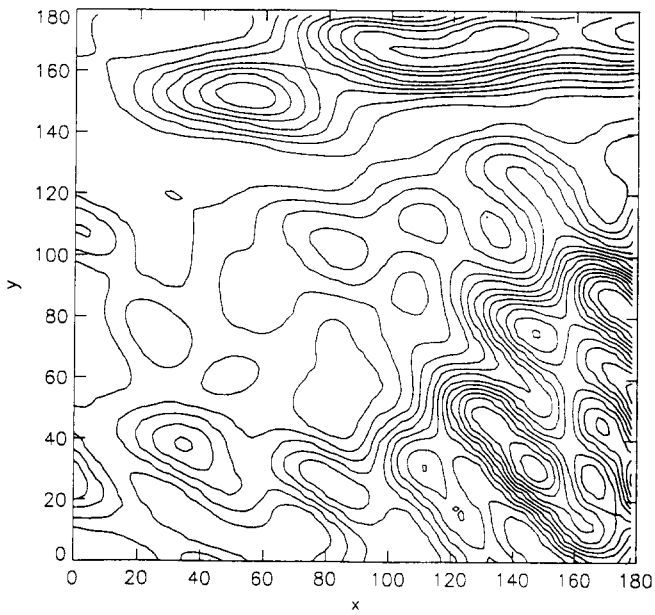

D

Fig. 7 (continued).

ing a defect's appearance. If, on the other hand, the local dynamics around the defects are similar to those observed in the mixing layer, one might expect the fundamental and subharmonic modes (and possibly others, too) to be phase-locked there.

There is clearly room, and opportunity, for further work. The wavelet analysis offers the possibility of searching for locally nonlinear dispersion relations, and for isolating the energy transfer mechanisms around these defect sites. The analogy with the mixing layer may, or may not, ultimately prove to be useful or appropriate. It will also be of interest to compare and contrast this perspective with the 'wave-crest pairing' mechanisms discussed by Ramamonjiarisoa and Mollo-Christensen (1979).

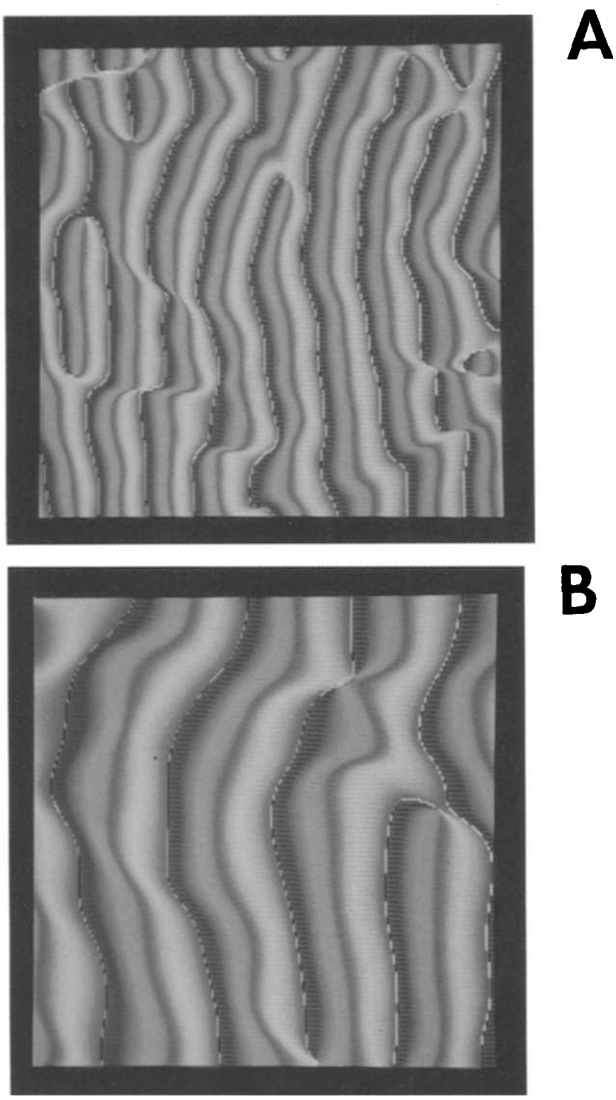

Fig. 8. The phase, $\angle f_{W_c}(a, b)$ for $a = 19$ (A) and $a = 38$ (B), corresponding to fundamental and subharmonic scales, respectively.

Measurement of the local dispersion relation, $\omega(\boldsymbol{k})$, and group velocity, $\boldsymbol{U}_g(\boldsymbol{k})$ of the various modes should allow some of these issues to be clarified, and can be achieved, in principle, if two or more wavelet cubes,

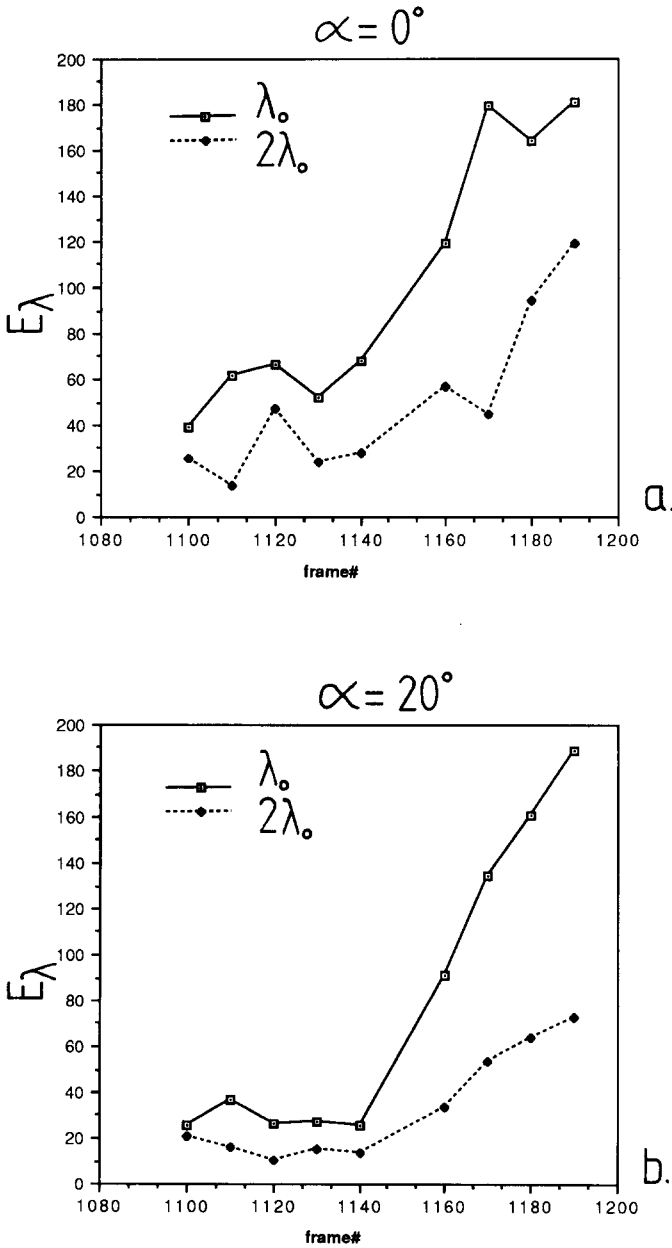

Fig. 9. E_{λ_0} and $E_{2\lambda_0}$ for the Morlet2D wavelet transform for $\alpha = 0°$ (a), and $\alpha = 20°$ (b), where α corresponds to the angle between the mean wind and the directional filter of Morlet2D.

separated by some small Δt, can be interrogated. Each single cube contains information on the most energetic scales at each spatial location, from $|f_W(a, \boldsymbol{b})|$. As, at any given scale, a, one can differentiate the corresponding phase fields with respect to time, $\omega = \Delta\phi/\Delta t$, one can obtain $\omega(\boldsymbol{k})$. A differentiation in space leads to $\boldsymbol{C}_g(\boldsymbol{k}) = \partial\omega/\partial\boldsymbol{k}$. Some extra complications arise in real data with noise, but work is in (good) progress on this problem.

4.3. Energy is transferred to wavevectors inclined to the wind direction

Finally, if one plots the isophase lines at slices corresponding to the fundamental and subharmonic wavelengths for the argument of the trans-

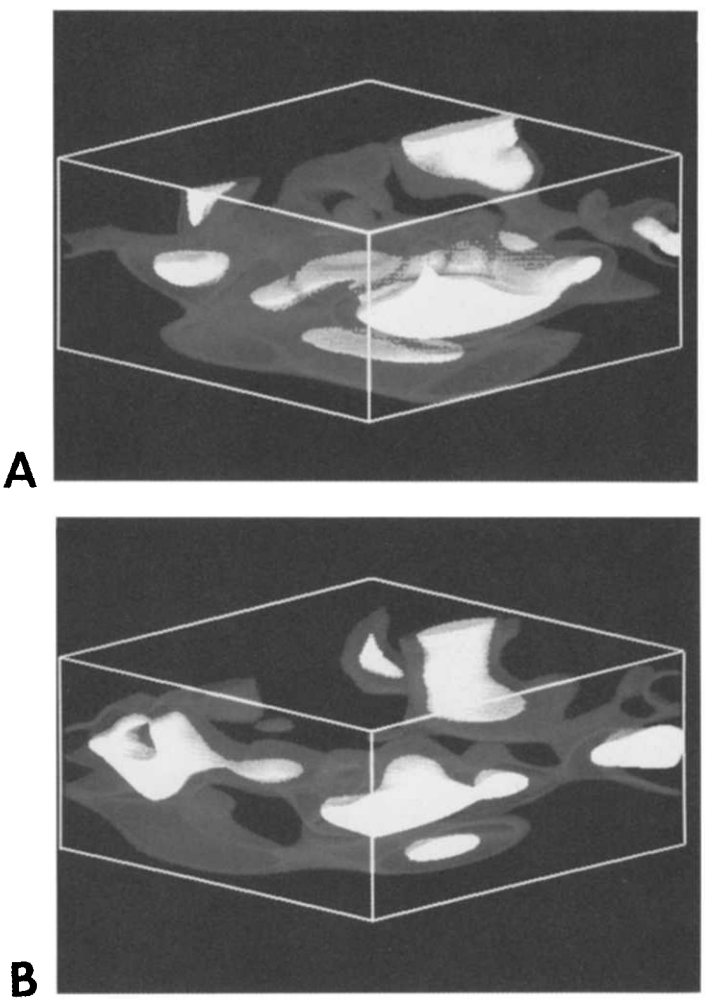

Fig. 10. (A) $|f_{W_\alpha}(a, \boldsymbol{b})|$, for $\alpha = 0°$ at early time (Fig. 3(a)). (B) For Fig. 3(b), about 1 s later (C) At later time, from Fig. 3(i). The cube orientation is as in Fig. 5.

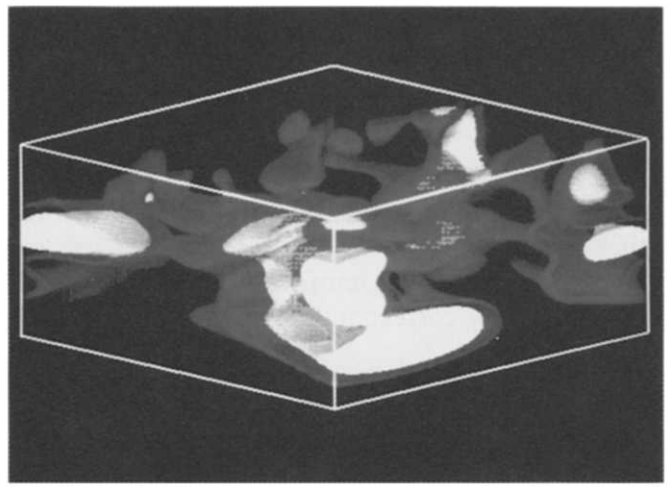

C

Fig. 10 (continued).

form at later times (Figs. 8(a) and 8(b) do this for timestep i of Fig. 3), it is apparent, first, that the dislocations or discontinuities in the isophase lines occur at both λ_0 and $2\lambda_0$. Second, phase lines are not all oriented normal to the original forcing (wind) direction, but many appear to be tilted by some small angle.

The Morlet2D wavelet can be used to select for wavevectors with a particular orientation, and following the indications of Fig. 8, from the Arc wavelet, the energy at fundamental (solid lines) and subharmonic scales is plotted for those wavevectors with orientation close to 0° (Fig. 9(a)) and for those with an angle of approximately 20° to the wind direction (Fig. 9(b)) Although the energy of the fundamental at 0° (the wavelet orientation $\alpha = 0$, denoted α_0) eventually saturates, as observed in the Arc result, those wavevectors resonating at α_{20} do not. The growth of the fundamental at α_{20} is slower than at α_0. Only one orientation angle, $\alpha = 20°$, based on the indications of the $\angle f_W(a, \boldsymbol{b})$ plots, was interrogated here, and it remains to survey the full range of plausible orientations. This result can be correlated with differences in the evolution of the spatial distribution of energy densities. Figures 10(a)–10(c) show three timesteps in $|f_{W_\alpha}(a, \boldsymbol{b})|$ for α_0 and Figs. 11(a)–11(c) show the corresponding results for α_{20}. There is a small tendency for the spatial intermittency of the energy at α_0 to increase with time, but the α_{20} component, on the other hand, clearly becomes more broadly distributed (less intermittent) in space over the same time period. The tilted wave component apparently is growing faster and occupying a larger portion of the (fixed) spatial domain. The physical significance of this is as yet unclear. It could be wholly or partly a

consequence of small asymmetries in the original wind-forcing. Nevertheless, the capacity of the WT to detect and quantify local energy densities in this fashion will be very valuable.

5. CONCLUDING REMARKS

The work described here represents the first few steps in quantifying the local nonlinear dynamics of small-scale wind-generated surface waves. Further progress will depend not only on improvements in experimental design and data analysis but also on corresponding advances in theoretical

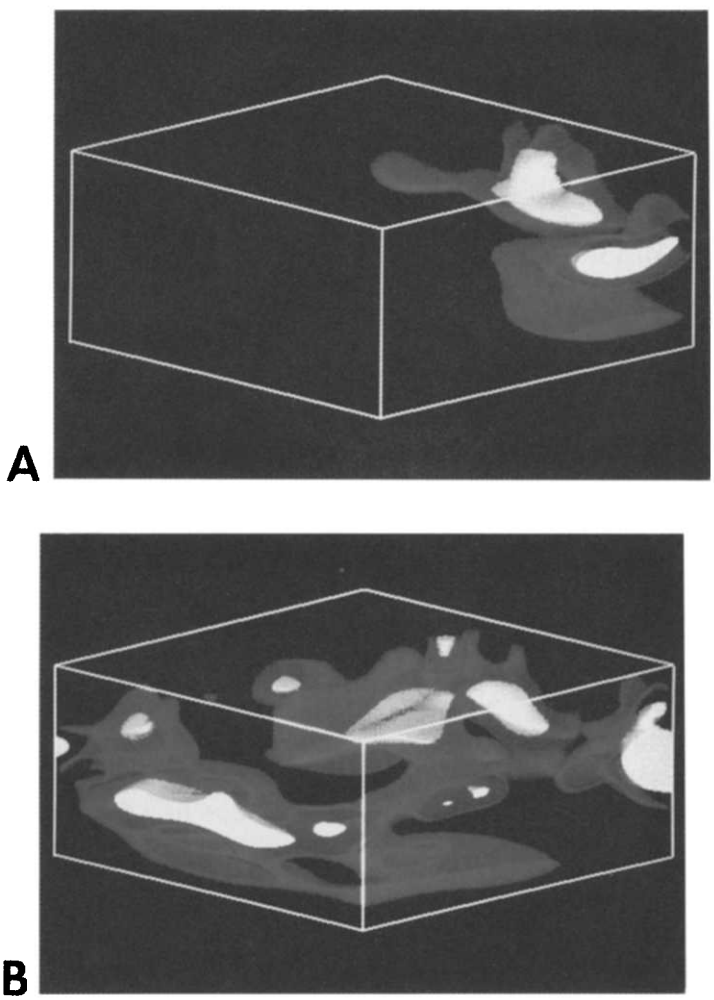

Fig. 11. Sequence as Fig. 10; $|f_{W_\alpha}(a, b)|$, for $\alpha = 20°$ at early (A), middle (B), and late (C) times.

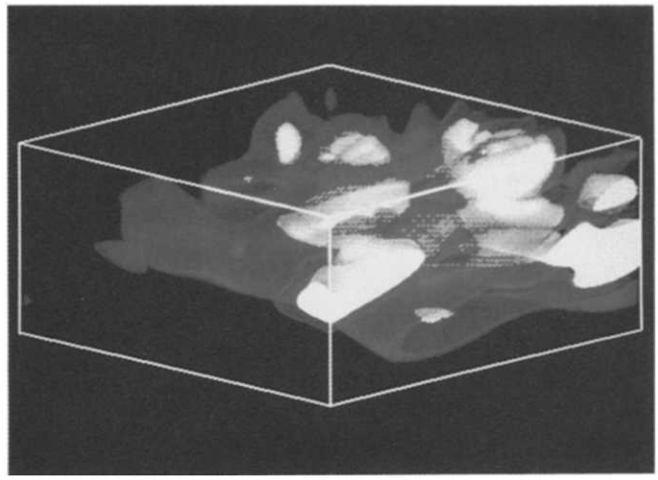

C

Fig. 11 (continued).

modelling, and subsequently careful comparisons between the two. It appears that a suitable nonlinear stability analysis, taking into account both the effect of finite-sized shear layers (in both fluids), and a density interface with surface tension, would be useful. The full problem is rather complicated, and involves the spatial and temporal growth of boundary layers in both fluids. The most complete theoretical analyses (see Valenzuela (1976) and Kawai (1979), and Creamer and Wright (1992) for added effect of surface contaminants) assume time-independent wind and water current profiles. A small, but helpful step, might be to modify the approach of Lawrence et al. (1991), who employed a piecewise linear approximation to the density and velocity profiles of a density stratified mixing layer. Caponi et al. (1992) also used a piecewise linear approximation to investigate the effects of water shear on the stability of the air–water interface, and offered specific predictions of regimes of instability mechanisms (of Miles' critical layer or Kelvin–Helmholtz type) at various wind speeds, and a detailed comparison ought to be possible with this type of model when quantitative data are available for a number of wind speeds.

It is planned to measure whole-field surface wave slopes in the NASA Wallops Fields wave tank, using a technique introduced by Jähne and Riemer (1990). In its present form, the apparatus gives the wave slope in one direction only, but simultaneously over the 2-D sampling area. Modifications and/or alternative techniques are being investigated so that the full range of wavevector directions can be measured at once, and the computations of $\omega(\boldsymbol{k})$ and $\boldsymbol{U}_g(\boldsymbol{k})$ can proceed as outlined above. The combination of non-direction-specific (Arc) and directional (Morlet2D) wavelet trans-

form analyses described here will assist in determining the range of angles that must be sampled in the first place.

REFERENCES

Caponi, E.A., Caponi, M.Z., Saffman, P.G. and Yuen, H.C. (1992). A simple model for the effect of water shear on the generation of waves by wind. Proc. R. Soc. London, Ser. A, 438: 95–101.

Combes, J.M., Grossmann, A. and Tchamitchian, P., 1989. Wavelets. Time–Frequency Methods and Phase Space. Springer-Verlag, Berlin.

Creamer, D.B. and Wright, J.A., 1992. Surface films and wind wave growth. J. Geophys. Res., C, 97: 5221–5229.

Dallard, T. and Browand, F.K., 1993. Scale transitions at defect sites in the mixing layer: application of the 2-D Arc wavelet transform. J. Fluid Mech., 247: 339–368.

Dallard, T. and Spedding, G.R., 1993. 2-D wavelet transforms: generalisation of the Hardy space and application to experimental studies. Eur. J. Mech. B/Fluids, 12: 107–134.

Farge, M., 1992. Wavelet transforms and their applications to fluid turbulence. Annu. Rev. Fluid Mech., 24: 395–457.

Farge, M. and Rabreau, G., 1988. Transformée en ondelettes pour détecter et analyser les structures cohérentes dans les écoulements turbulents bidimensionnels. Méc. Fluides, 307: 1479–1486.

Gabor, D., 1945. Theory of communication. J. Inst. Electr. Eng., 93: 429–457.

Geernaert, G.L. and Plant, W.J., 1990. Surface Waves and Fluxes. Part 1. Current Theory. Part 2. Remote Sensing. Kluwer Academic, Dordrecht.

Grossmann, A. and Morlet, J., 1984. Decomposition of Hardy functions into square integrable wavelets of constant shape. SIAM J. Math. Anal., 15: 723–736.

Grossmann, A., Kronland-Martinet, R. and Morlet, J., 1989. Reading and understanding wavelet transforms. In: J.M. Combes, A. Grossmann and P. Tchamitchian (Editors), Wavelets, Time–Frequency Methods and Phase Space. Springer-Verlag, Berlin, pp. 2–20.

Jähne, B., 1991. Digital Image Processing. Concepts, Algorithms and Scientific Applications. Springer-Verlag, Berlin.

Jähne, B. and Riemer, K., 1990. Two-dimensional wave number spectra of small-scale water surface waves. J. Geophys. Res., C, 95: 11531–11546.

Kawai, S., 1979. Generation of initial wavelets by instability of a coupled shear flow and their evolution to wind waves. J. Fluid Mech., 93: 661–703.

Lawrence, G.A., Browand, F.K. and Redekopp, L.G., 1991. The stability of a sheared density interface. Phys. Fluids, A., 3: 2360–2370.

Liandrat, J. and Moret-Bailly, F., 1990. The wavelet transform: some applications to fluid dynamics and turbulence. Eur. J. Mech. B/Fluids, 9: 1–19.

Melville, W.K., 1983. Wave modulation and breakdown. J. Fluid Mech., 128: 489–506.

Miles, J.W., 1957. On the generation of surface waves by shear flows. J. Fluid Mech., 3: 185–204.

Miles, J.W., 1959. On the generation of surface waves by shear flows. Part 2. J. Fluid Mech., 6: 568–582.

Murenzi, R., 1989. Wavelet transforms associated with the N-dimensional Euclidean group with dilatations. In: J.M. Combes, A. Grossmann and P. Tchamitchian (Editors), Wavelets, Time–Frequency Methods and Phase Space. Springer-Verlag, Berlin, pp. 239–246.

Okuda, K., 1982a. Internal flow structure of short wind waves. Part 1. On the internal vorticity structure. J. Oceanogr. Soc. Jpn., 38: 28–42.

Okuda, K., 1982b. Internal flow structure of short wind waves. Part 2. The streamline pattern. J. Oceanogr. Soc. Jpn., 38: 313–322.

Okuda, K., 1982c. Internal flow structure of short wind waves. Part 3. Pressure distribution. J. Oceanogr. Soc. Jpn., 38: 331–338.

Phillips, O.M., 1957. On the generation of waves by turbulent wind. J. Fluid Mech., 2: 417–445.

Phillips, O.M., 1977. The Dynamics of the Upper Ocean. Cambridge University Press, Cambridge.

Phillips, O.M., 1988. Remote sensing of the sea surface. Annu. Rev. Fluid Mech., 20: 89–109.

Ramamonjiarisoa, A. and Mollo-Christensen, E., 1979. Modulation characteristics of sea surface waves. J. Geophys. Res., C, 84: 7769–7775.

Riemer, K., 1991. Analyse von Wasseroberflächenwellen im Orts-Wellenzahl-Raum. Dissertation, University of Heidelberg.

Snyder, R.L., Dobson, F.W., Elliot, J.A. and Long, R.B., 1981. Array measurements of atmospheric pressure fluctuations above surface gravity waves. J. Fluid Mech., 102: 1–59.

Spedding, G.R., Dallard, T. and Browand, F.K., 1993. The design and applications of 2D wavelet transforms for fluid turbulence data analysis. In: Wavelets and Turbulence, Proc. DARPA/ONERA Summer Workshop, Princeton, NJ, June 1991, in press.

Valenzuela, G.R., 1976. The growth of gravity–capillary waves in the coupled shear flow. J. Fluid Mech., 76: 229–250.

Wu, H.Y., Hsu, E.Y. and Street, R.L., 1979. Experimental study of non-linear wave–wave interaction and white-cap dissipation of wind-generated waves. Dyn. Atmos. Oceans, 3: 55–78.

Yang, R., Browand, F.K., Coullet, P. and Huerre, P., 1993. A model of defect-induced pairing in mixing layers. J. Fluid Mech., 248: 403–423.